The behaviour of nematic liquid crystals in chemically patterned millimetre-sized rectangular surfaces

Abigail Bond, Thomas Moorhouse, Sally A. Peyman & Helen F. Gleeson

View supplementary material ↗

Published online: 28 Apr 2025.

Submit your article to this journal ↗

Article views: 368

View related articles ↗

View Crossmark data ↗

Taylor & Francis
Taylor & Francis Group

The behaviour of nematic liquid crystals in chemically patterned millimetre-sized rectangular surfaces

Abigail Bond [iD], Thomas Moorhouse [iD], Sally A. Peyman [iD] and Helen F. Gleeson [iD]

School of Physics and Astronomy, University of Leeds, Leeds, UK

ABSTRACT

We describe a method to produce nematic liquid crystal 'semi-droplets' with potential use in sensing by chemically patterning rectangles on solid surfaces, surrounded by a hydrophobic monolayer to confine the liquid crystal. The substrate has directional planar anchoring, while the top surface is a liquid crystal/air interface. The effects of varying the semi-droplet of E7 height between ~20 and 420 μm; aspect ratios between 0.5 and 1; widths between 6 and 13 mm and lengths between 6 and 20 mm were investigated, significantly extending the range of semi-droplets considered in the literature; their increased size is expected to be useful in real-life devices. A geometric model for the semi-droplet was derived and compared with an existing theoretical model, offering a simple method to predict the semi-droplet interface angle, which can subsequently be used to predict the maximum height and height variation along the semi-droplet. Polarised light imaging was used to deduce the semi-droplet height profile using the liquid crystal's birefringent properties, with excellent agreement with the model for heights ≤ 50 μm, even when the semi-droplet width was larger than E7's capillary length. It is suggested that the confinement surface is reusable by washing with the relatively cheap and safe solvent isopropanol.
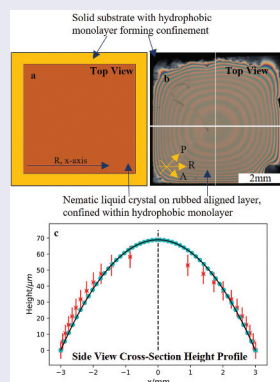
Introduction

A growing number of liquid crystal-based sensors [1], most coming after the seminal work of Gupta *et al.* [2], are being proposed because of their fast-responding, sensitive detection potential, many of which make use of nematic liquid crystals (NLC) as birefringent fluids that exhibit orientational order over relatively large distances. Such sensors typically rely on the effect whereby a small perturbation at the surface of the bulk NLC, such as the interaction of an analyte, can cause a change in the director field that is readily observed under polarised light. There are some excellent reviews that summarise the recent liquid crystal sensor literature [3–5]. Some recent examples of common confinement geometries of NLC in such sensors include droplets [6–16], in a NLC cell [17–22] or the NLC in contact with aqueous solutions [23–28]. Some other liquid crystal-based sensing examples reported include the use of whispering gallery mode resonances [29] or polymer-stabilised NLC [30]. The confinement shapes in this work are rectangles with aspect ratios between 0.5 and 1; however, a review that

This article has been corrected with minor changes. These changes do not impact the academic content of the article.

ⓘ Supplemental data for this article can be accessed online at https://doi.org/10.1080/02678292.2025.2489426

describes the effect of varying confinement geometries is given by Shin *et al.* [31]. Work on confinement of NLCs in rectangle-like geometries has been considered both experimentally and theoretically [32–40].

The motivation for investigating the confinement behaviour in this work is to explore the potential of a polarised light imaging-based NLC sensing device fabricated using carefully designed, 'semi-droplets' of NLC constrained onto a substrate, with one open-to-air surface. Figure 1 shows the confinement shape for the method presented in this work which uses rubbed polyimide[1] to produce a directional, planar alignment layer, together with contact photolithography using a bespoke photomask to define a wide range of rectangular shapes with known dimensions. A hydrophobic monolayer contains the NLC with the top surface open to air at ambient pressure. Such an approach has potential as a simple-to-use sensor, without the need for complex geometries or microdroplet fabrication that are a feature in many other cases. The reusability of the patterning surfaces in this work, which can be suggested due to a lack of significant change in the sample quality after washing with the relatively inexpensive and non-hazardous solvent isopropanol (IPA), is then a step towards cheaper and more sustainable NLC-based sensing methods. However, the ability to understand the effect of varying the confinement dimensions and height of the confined NLC is important to the design, that is the focus of this work.

The recent papers by Bao *et al.* [38] and Cousins *et al.* [39] form the motivation for our current work. Bao *et al.* [38] produced stripes using a direct-write laser, O_2 plasma etching and deposition of a self-assembled monolayer, with no specific alignment layer on the LC-containing area. Cousins *et al.* [39] utilised rubbed poly (vinyl alcohol) (PVA) as an alignment layer, with confinement created from Teflon surrounding the rectangle. In Bao *et al.*, the stripes are 10–30 μm in width (with a height for the 30 μm stripes of 1.22 μm), which is of a different order of magnitude to that in Cousins *et al.*, who employ a width:length of 1.2:60 mm. Both studies use geometries that are much less than the capillary

length of the nematic liquid crystals used. Bao *et al.* consider a single semi-droplet height, while Cousins *et al.* record two situations of ~1 μL and 3 μL NLC dispense volumes into their confinement area. Bao *et al.* present an equation for the maximum height of the confined NLC, and Cousins *et al.* present a model to describe the height variation across the width of the confined NLC. The current work is directly compared to the assumptions that Cousins *et al.* make for their semi-droplet, and the equation they use to describe the height variation across a semi-droplet that they assume to be isotropic.

Clearly, the dimensions of the confined NLC semi-droplet in any application will be important and this work considers a significant expansion of the semi-droplet dimension; confinement shapes between 0.5 and 1 in aspect ratio, 6–13 mm in width, and 6–20 mm in length, with NLC heights between ~20–420 μm were investigated using polarised light images. This wide-ranging study works towards optimisation of these parameters for future use in sensors, considering , specifically, what dimensions offer high-quality and readily observable director fields. We derive a simple geometric model in which the key parameter is the interface angle at the edge of the confinement region and consider it with respect to the model deduced by Cousins *et al.* [39] which employs the cross-sectional area of the confined NLC. Combining the models allows the cross-sectional area, estimated using the NLC semi-droplet volume and assuming a constant cross-sectional area along the confinement length to be used to predict the semi-droplet interface angle. This itself is powerful with our model as the height variation and maximum height can therefore be predicted.

Geometric modelling of the semi-droplets

A large amount of work on modelling of semi-droplets of NLCs has been undertaken by Cousins *et al.* [39] who presented an in-depth theoretical description of a specific case of general equations described in an earlier paper [41] on confined NLC
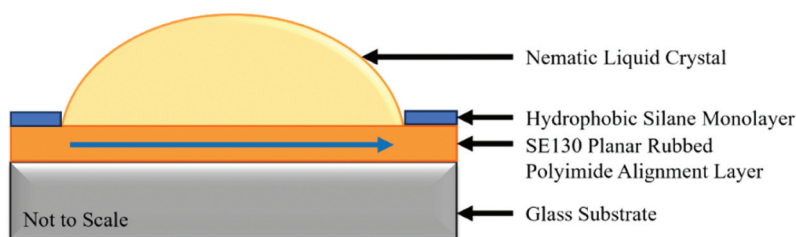

Figure 1. (Colour online) Schematic side-view of confined NLC semi-droplet in chemically patterned rectangles. The NLC is confined between hydrophobic monolayer regions and sits on a planar rubbed polyimide alignment layer. The blue arrow represents the rubbing direction of the alignment layer. The schematic is not to scale.

within a rectangular geometry with a solid aligning surface and an open air/NLC interface, assuming the NLC is static and can be treated as 2D. Cousins et al. [39] pinned this NLC semi-droplet at the edges, assumed it to be a thin semi-droplet with symmetry about x = 0 and allowed for the assumption that the effects of gravity on the semi-droplet were negligible by ensuring that the semi-droplet half-width, d, is much smaller than the capillary length, L_C, i.e. $d \ll L_c = \left(\frac{\gamma}{\rho g}\right)^{\frac{1}{2}}$ [42], where γ is the NLC/air interfacial tension, ρ is the NLC density and g is the gravitational acceleration. For their experimental semi-droplet, Cousins et al. [39] filled a 2d = 1.2 mm, and length, L = 60 mm confinement area with ~1 µL or ~3 µL of the NLC 5CB. Their confinement was formed using a rubbed alignment layer of PVA surrounded by Teflon. They experimentally validated Equation (1) as the height variation at the very edge of their experimental semi-droplet (x = 400–600 µm), assuming the material was isotropic, static and with a well-defined edge-pinning position,

$$h(x) = \frac{3\varepsilon(d^2 - x^2)}{4d} = \frac{3V(d^2 - x^2)}{4d^3 L}. \qquad [1]$$

In Equation (1), h(x) is the height variation across the semi-droplet's x-axis, A is the cross-sectional area, L is the length and V is the NLC volume of the semi-droplets. $\varepsilon = \frac{A}{d^2}$ and it is assumed that $\frac{A}{d^2} \ll 1$, implying the semi-droplet is thin.

The work by Cousins et al. [39] is extremely detailed, theoretically describing the confined NLC semi-droplets in relation to important NLC properties such as the elastic energy of the director field, different possible director field orientations, and anchoring strength. However, in this work, we seek to present a simple geometric model that describes the height variation across the width of the semi-droplet, with a focus on experimental parameters. Like Cousins et al.'s semi-droplet isotropic model (Equation (1)), our model does not consider gravity and is static. In addition, in this current work, it is expected that ε ~0.007–0.2, therefore largely matching the assumptions used in Equation (1). The model we present is not liquid crystal-specific, further simplifying the description of the semi-droplet and making it broadly applicable. In this work, d = 3–6.5 mm which is somewhat greater than the capillary length for the NLC E7, L_c ~1.57 mm (calculated using $\gamma = 24.2 \times 10^{-3}$ Nm^{-1} [8], $\rho = (0.97-1) \times 10^3$ kgm^{-3} [2] and g = 9.81 ms^{-2}). This contrasts to the assumption in Cousins et al. [39] where $d \ll L_c$, therefore can be used as a comparison
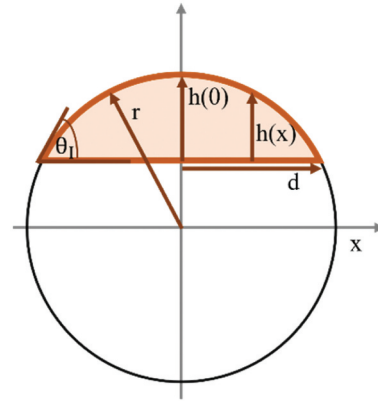

Figure 2. (Colour online) Diagram of the geometric model parameters used to describe the cross-section of an NLC 'semi-droplet' confined in a rectangular geometry showing the maximum height, h(0); variation of height with x, h(x); half-width of the stripe, d; radius of the circle from which the confined NLC shape is formed, r, and interface angle, θ_I. The distance 2d is the length of the minor chord of the circle and the shaded area is the cross-sectional area of the semi-droplet, A. The height of the semi-droplets in this work are of the order of 10–500 of µm, and the radius of the circle is of the order of 10–100 of mm.

to see where the assumption of negligible gravitational contributions breaks down.

To form our simple geometric model, we assume that the base of the semi-droplets with width 2d, are chords of a circle and the height is therefore described by the minor arc of the minor segment of a circle with radius r, as shown in Figure 2. Then, Equation (2),

$$h(x) = d\left(\frac{\alpha}{\sin(\theta_I)} - \frac{1}{\tan(\theta_I)}\right), \qquad [2]$$

where,

$$\alpha = \left[1 - \left(\frac{x\sin(\theta_I)}{d}\right)^2\right]^{\frac{1}{2}},$$

describes the variation in height of the semi-droplet, h(x), across the confinement width, x. We denote the angle that the NLC makes with the surface at the confinement edge as the interface angle, θ_I, noting that this is not the same as the contact angle of NLC on the polyimide surface since the NLC cannot spread freely due to the confinement shown in Figure 1. To show this, a droplet of E7 was placed onto homogeneous SE130 or silane coated onto glass. On the former, the droplet spread to a very thin layer, whereas on the silane, the droplet shape was retained, with a contact angle of 70° ± 2°.

It is assumed in this work that the cross-sectional area of the semi-droplet is constant along the confined length

and therefore can be determined from the volume of the NLC, known from the dispensing conditions to be between 0.5 and 30 μL, i.e. V = AL. In such case, it is simple to see in Equation (1) that the NLC maximum height should vary linearly with V. This is useful as the key experimental parameters in this work are the rectangle's size and the dispense volume of the NLC.

Equating our simple geometric model, Equation (2), with Cousins et $al.$'s [39] isotropic semi-droplet model, Equation (1), at x = 0 provides Equation (3),

$$\theta_I = 2\cot^{-1}\left(\frac{4}{3\varepsilon}\right). \qquad [3]$$

This allows for a simple method to predict the interface angle, which itself a powerful tool to predict other properties of the semi-droplet, as Equation (1) describes the semi-droplet height in terms of its cross-sectional area, whereas Equation (2) describes height in terms of θ_I. The known properties of the NLC semi-droplets as formed are V, d and L, meaning A can be estimated (assuming uniform filling) using V = AL. This in turn can be used with d to predict ε with Equation (1), which can then be used with Equation (3) to predict θ_I. This method to predict θ_I is necessary as it would be impractical to measure some of the smaller interface angles. When θ_I is substituted into Equation (2) at x = 0, the maximum semi – droplet height is predicted, or with substitution into Equation (2), h(x) can be predicted.

Although it is not discussed in-depth in this current work, the interface angle could alternatively be used with the simple geometric equation given by Equation (4) to predict the radius of the circle shown in Figure 2,

$$r = \frac{d}{\sin(\theta_I)}. \qquad [4]$$

Summarising, the model given by Cousins et $al.$ [39] for a thin semi-droplet that is symmetric about x = 0, for an isotropic material within a well-defined confinement area is compared to the geometric model derived here (with the same assumptions), which was created as a simpler approach to describe the shape of the semi-droplets. However, unlike in Cousins et $al.$ where $d \ll L_C$, in this work $d > L_C$. We experimentally determine the height across the whole semi-droplet width and consider whether the model breaks down due to the comparable sizes of the half-width and capillary length. Equation (1) can be used in conjunction with Equation (2) to provide a simple route for predicting θ_I, which is a valuable property to allow many other properties of the semi-droplets to be predicted.

Methods and materials

Chemical patterning

Glass microscope slides were cleaned in an ultrasonic bath in deionised water with Decon-90, followed by separate washes in deionised water and acetone. Planar polyimide SE130 with a pretilt of ~2° (Nissan Chemical Industries, Ltd.) was deposited via spin-coating, dried, cured and machine rubbed using a velvet roller before Microposit® S1813® photo resist (Shipley) was deposited via spin-coating. Rectangular shapes were then patterned into the photoresist layer via contact photolithography, with a bespoke photomask. The patterns were then developed in a Microposit® MF® CD-26 developer solution (Shipley) and then rinsed in deionised water. UV exposure of the whole sample with no photomask was completed, before being placed in an oven at 100°C for a minimum of 15 minutes. 1H,1H,2H,2H-Perfluorooctyltrichlorosilane 97% (Thermo Scientific) was deposited onto the surface in a desiccator where nitrogen gas was passed over the samples, before being left under vacuum for ~1 hr [43,44]. Any remaining photoresist was removed and rinsed using IPA and deionised water. The key steps of this process are shown schematically in Figure 3.

NLC deposition

The NLC, E7 (Synthon), was used to fill the confinement areas as follows. A vial containing the NLC was placed alongside the chemically patterned substrate on a hotplate above the nematic-to-isotropic temperature, T_{NI} (~60°C), before the NLC was pipetted using specifically measured volumes onto the confinement areas of the substrate. The NLC was spread to the confinement edges using directional compressed air or gentle tilting as required, before removing the sample from the heat. The sample was again heated above T_{NI}, held at a constant temperature, and cooled on a hot stage to remove any air bubbles before imaging. The surfaces were used multiple times, and between each new dispense of NLC, the 'old' NLC was removed from the surface with IPA, before drying with compressed air and/or evaporation on a hotplate.

Imaging

The macroscopic sample areas considered in this work were too large to image using a typical polarising microscope. Therefore, to image the NLC samples using polarised light, a bespoke imaging system was created to image with a large field of view between ~15 and 94 mm. The resolution of 9.26–27.78 μm is such that there is little
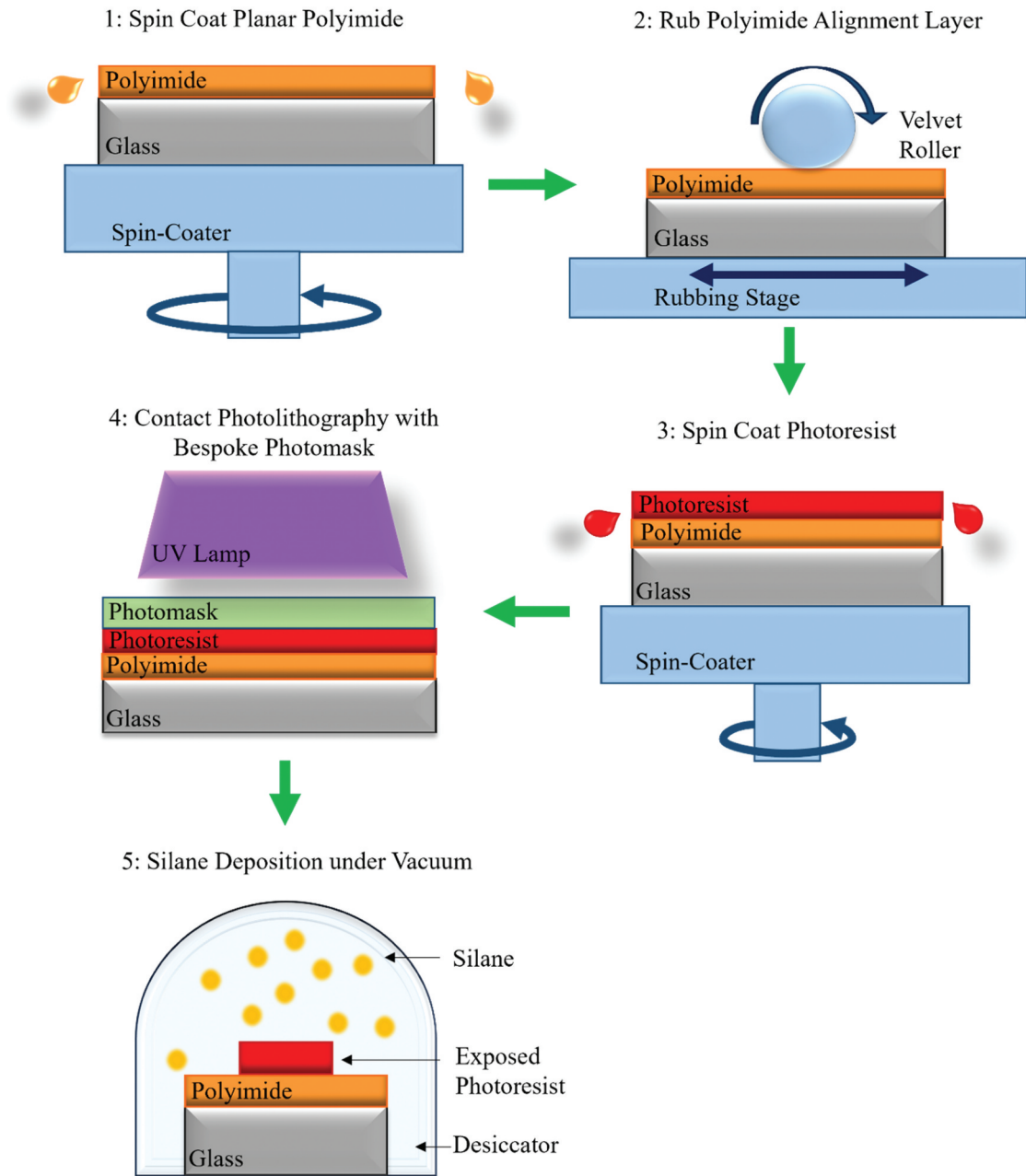
1: Spin Coat Planar Polyimide

Polyimide

Glass

Spin-Coater

2: Rub Polyimide Alignment Layer

Velvet Roller

Polyimide

Glass

Rubbing Stage

4: Contact Photolithography with Bespoke Photomask

UV Lamp

Photomask
Photoresist
Polyimide

Glass

3: Spin Coat Photoresist

Photoresist
Polyimide

Glass

Spin-Coater

5: Silane Deposition under Vacuum

Silane

Exposed Photoresist

Polyimide

Desiccator

Glass

Figure 3. (Colour online) Key steps in the fabrication of the chemically patterned glass for NLC confinement in rectangles to form 'semi-droplets'. The schematics are not to scale.

compromise with the quality of the images. The imaging apparatus can be used with no polariser, one or two polarisers, and in both transmission and reflection modes. This set-up allows images to be recorded under a variety of illumination and polarisation conditions. Further fabrication and imaging details can be found in the *supplementary information*.

Measurement of semi-droplet height

The birefringence of the confined NLC could be readily imaged when the rubbing axis of the confinement was held at 45° to the crossed polarisers in the imaging system, as can be seen in Figure 4(a) which shows typical data. To experimentally validate the models presented in the previous section, the height of the semi-droplet was measured across its width and length by observing the number of pink birefringence fringes in the image. These fringes satisfy the full-wave condition of the birefringent NLC for green wavelengths; green is absorbed by the analyser, and pink passes through. This full wave condition can be written in terms of the height $h = \frac{m\lambda}{\Delta n_{eff}}$, where $m \in \mathbb{Z}$, the first fringe closest to the
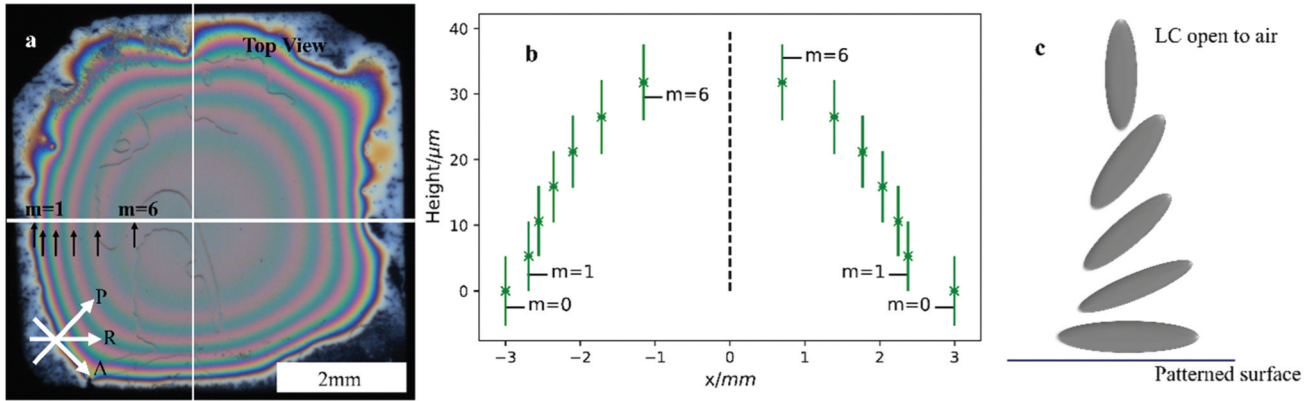
Figure 4. (Colour online) (a) Top view polarised light image of 0.5 μL NLC confined in 6 mm square chemically patterned surface with top surface open to air. The value of m represents the number of pink birefringent fringes, counting from the semi-droplet edge. P, A and R show the relative directions of the polariser, analyser and rubbing, respectively. White lines show the cross-section along which the centre-to-centre distances of the fringes have been measured to deduce the height variations. The scale bar is 2 mm. (b) Plot of the centre-to-centre distances of the pink birefringent fringes along the width marked by a white line in (b), with their corresponding measured heights. (c) Hybrid-aligned nematic section which is used to estimate the effective birefringence of the NLC semi-droplets confined within rectangles. The pretilt at the solid substrate/NLC interface is assumed to be 2° and homeotropic alignment is assumed at the NLC/air interface.

droplet edge corresponds to $m = 1$ and a green wavelength of $\lambda = 0.53 \pm 0.04 \mu m$ is assumed.

The effective birefringence of the sample, Δn_{eff}, can be calculated by assuming a hybrid aligned nematic (HAN) director variation within the semi-droplet (Figure 4(c)), with a small pretilt planar alignment (~2°) at the solid substrate, and homeotropic orientation at the NLC/air interface. The HAN director field is a good approximation across the cross-section of the semi-droplets as the semi-droplet heights are approximately three orders of magnitude smaller than the radius of the circle they are modelled on (Figure (2)), with a small region near x = ±d where the assumption will break down. The extraordinary and ordinary refractive indices of E7 are taken as $n_e = 1.73$ and $n_o = 1.52$, respectively, at approximately 25°C [45], giving $\Delta n_{eff} = 0.1$ (see the *supplementary information* for the full calculation). Figure 4(a) shows a typical sample where a 6 mm square confinement size is filled with V = 0.5 μL E7 and six birefringent fringes can be seen. Counting from the edge, where the first fringe is $m = 1$, and using $h = \frac{m\lambda}{\Delta n_{eff}}$, the height profile can be measured as indicated in Figure 4(b), in this case with a maximum height of h = 32 ± 6 μm.

A factor to consider when evaluating what contributes to an 'optimum' semi-droplet height for sensing is that alignment layers for NLCs are typically only effective up to a layer thickness of ~100 μm from the anchoring condition. Therefore, for the taller semi-droplets, there may be some disorder in the centre of the confined NLC which would make the HAN director field

assumed in Figure 4(c) less accurate in the central regions and therefore have some effect on Δn_{eff}.

Results and discussion

Semi - droplet height

Figure 5 shows polarised light images of samples with varying NLC semi-droplet heights, produced by dispensing different volumes of material into the 6 mm square confinement size. Examples of 11 mm square, 16 × 13 mm rectangular and 20 × 10 mm rectangular confinements, also with varying semi-droplet heights are given in Figures 6 and S3.

Figure 5(a–d), Figure 6(a-c,e-g,i-l) and Figure S3(a,b, g,h) show clear birefringent fringes that allow for measurements of the height across the semi-droplets as described. ε, the interface angle and the maximum height can all be predicted from the dispensed volume of the NLC and geometric equations, as was described in the section on modelling. Figure 7 compares the experimentally determined height with the predicted height for these semi-droplets, removing geometric effects by scaling the volume of dispensed NLC by the surface area of each confinement size, $\frac{V}{2dL}$. Figure 7(a) shows that the heights predicted using the model are in good agreement with the experimental data, i.e. within three uncertainties (Figure 6(l)), two uncertainties (Figure 5(a,c)) and Figure 6(b,i-k) or, as is the case for the majority of the samples, within one uncertainty, across the different
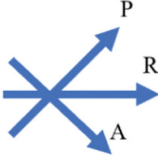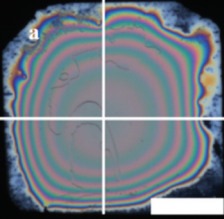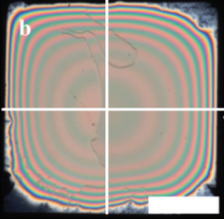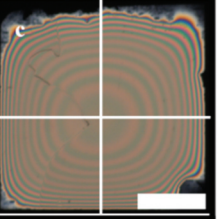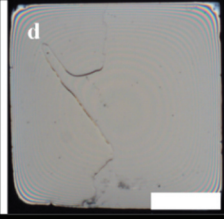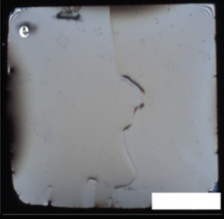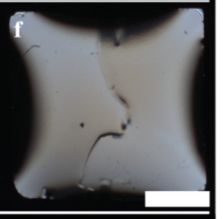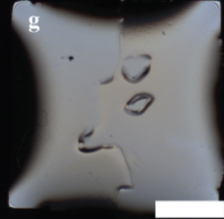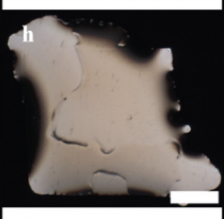
NLC Volume, V/μL	0.5 ± 0.01	1 ± 0.01	1.8 ± 0.01
Measured height, h/μm	32 ± 6	42 ± 6	58 ± 7
Predicted height, h/μm	21 ± 1	42 ± 2	75 ± 3

NLC Volume, V/μL	3 ± 0.01	5 ± 0.01	7 ± 0.01
Measured height, h/μm	110 ± 10	-	-
Predicted height, h/μm	125 ± 6	208 ± 9	290 ± 10

NLC Volume, V/μL	8 ± 0.01	9 ± 0.01	10 ± 0.01
Measured height, h/μm	-	-	-
Predicted height, h/μm	330 ± 10	380 ± 20	420 ± 20

Figure 5. (Colour online) Polarised light imaging of varying NLC 'semi-droplet' volumes confined in 6 mm squares on chemically patterned surfaces with a rubbed alignment layer on a solid substrate and an NLC/air interface. Maximum heights measured using pink birefringent fringes are compared to those predicted from calculation of the semi-droplet cross-sectional area (V = AL), leading to predictions of ε (Equation (1)), interface angle (Equation (3)) and finally, height (Equation (2)). White lines show the cross-sections along which the centre-to-centre distances of the fringes have been measured to deduce the height variations across the semi-droplet width and length. The rubbing direction is at 45° to the crossed polarisers, with arrows marked P, A and R to show the relative directions of the polariser, analyser and rubbing respectively. The scale bars are 2 mm. The cropping of the images was varied to ensure that the field of view required to capture all the information (e.g. any overflowing liquid crystal) to be retained while maximising the image visibility.

confinement dimensions and NLC volumes. It is expected that the data should fall on a straight line with gradient $\frac{3}{2}$ (Equation (1)), and this is also shown in the figure. Therefore, we can conclude that our simple model can be used to predict the height of the semi-droplet from the dispense volume reasonably well.

Figure 7(b) shows the fractional difference, Equation (5), between the experimentally measured maximum height of the semi-droplets and those predicted from the models,

$$\text{Fractional difference} = \frac{h \text{ measured} - h \text{ predicted}}{h \text{ measured}}. \quad [5]$$

Considering this fractional difference, despite the good agreement in the height information (Figure 7(a)), there remain some systematic differences, especially for some of the larger rectangles used, highlighted in Figure 7(b), that need to be accounted for.

One possibility for this discrepancy is that some samples are clearly underfilled (e.g. Figure 5(a)) and some are
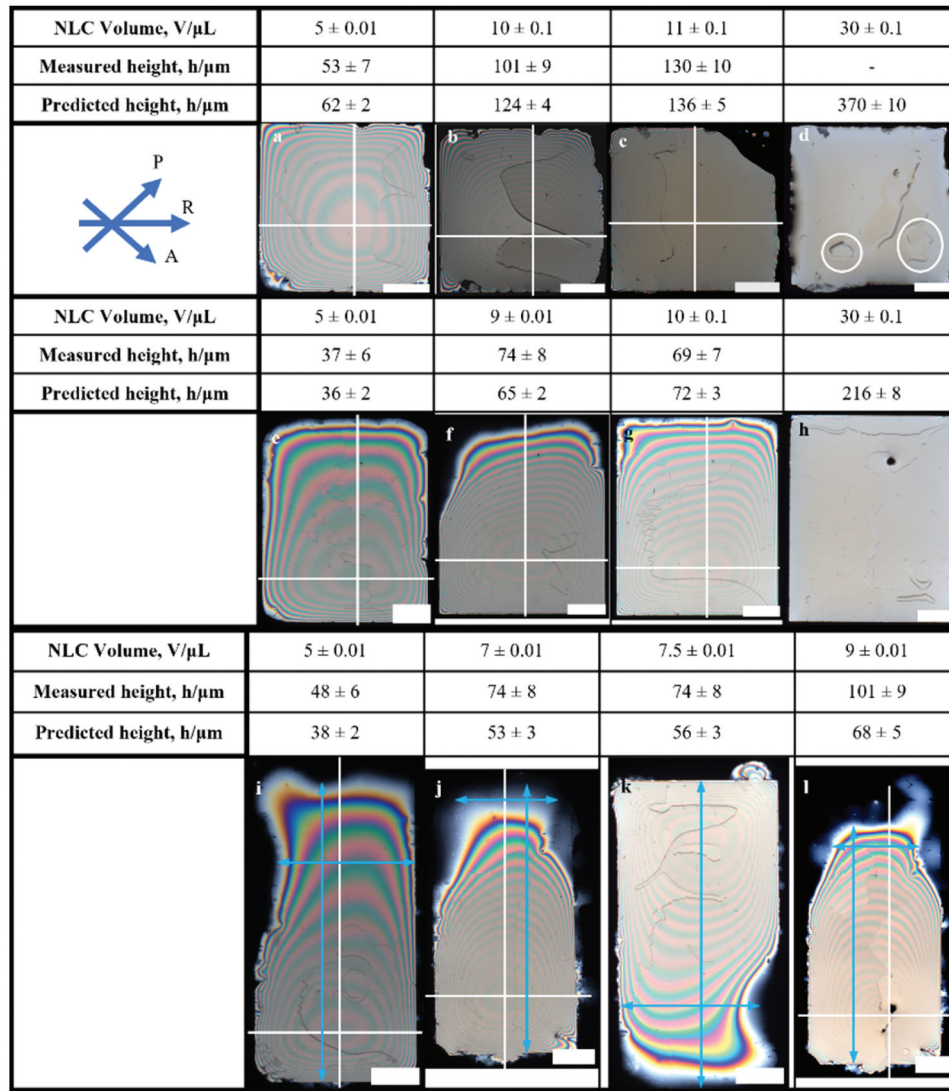
NLC Volume, V/µL	5 ± 0.01	10 ± 0.1	11 ± 0.1	30 ± 0.1
Measured height, h/µm	53 ± 7	101 ± 9	130 ± 10	-
Predicted height, h/µm	62 ± 2	124 ± 4	136 ± 5	370 ± 10

NLC Volume, V/µL	5 ± 0.01	9 ± 0.01	10 ± 0.1	30 ± 0.1
Measured height, h/µm	37 ± 6	74 ± 8	69 ± 7	
Predicted height, h/µm	36 ± 2	65 ± 2	72 ± 3	216 ± 8

NLC Volume, V/µL	5 ± 0.01	7 ± 0.01	7.5 ± 0.01	9 ± 0.01
Measured height, h/µm	48 ± 6	74 ± 8	74 ± 8	101 ± 9
Predicted height, h/µm	38 ± 2	53 ± 3	56 ± 3	68 ± 5

Figure 6. (Colour online) Polarised light images of varying NLC 'semi-droplet' volumes confined in rectangles on chemically of varying dimensions: (a-d) 11 × 11 mm; (e-h) 16 × 13 mm; (i-l) 20 × 10 mm, on patterned surfaces with a rubbed alignment layer on a solid substrate and a NLC/air interface. Maximum heights measured using pink birefringent fringes are compared to those predicted from calculation of the semi-droplet cross-sectional area (V = AL), leading to predictions of ε (Equation (1)), interface angle (Equation (3)) and finally, height (Equation (2)). White lines show the cross-sections along which the centre-to-centre distances of the fringes have been measured to deduce the height variation across the semi-droplet width and length. Blue lines show the width and length measured to approximate the true surface area of NLC. The rubbing direction is at 45° to the crossed polarisers, with arrows marked P, A and R to show the relative directions of the polariser, analyser and rubbing respectively. The scale bars are 3 mm. Extra domains are sometimes seen when the confinement is overfilled, as circled in (d) as an example. The cropping of the images was varied to ensure that the field of view required to capture all the information (e.g. any overflowing liquid crystal) to be retained while maximising the image visibility.

overfilled (e.g. Figure 5(h)) and in such cases, assuming that d and L are accurately known is somewhat questionable. The blue lines on Figure 6(i-l) for 20 × 10 mm confinement sizes show where the sizes of d and L were measured directly to obtain a more accurate NLC coverage surface area within the rectangle. These four samples were chosen because, as a confinement size group of samples, they have the worst agreement in general between the measured and predicted maximum heights,

where Figure 6(i-k) agree within two uncertainties, and Figure 6(l) agrees within three uncertainties. The samples in Figure 6(i-l) are marked in Figure 7(b). The maximum height was predicted in the same way using the models (i.e. estimating A from V = AL, then predicting ε, followed by θ_I and finally height at x = 0), but with the measured d and L values, and compared to the fractional difference for the heights assuming known d and L values (Figure 7(b)). In all cases, using the measured d and
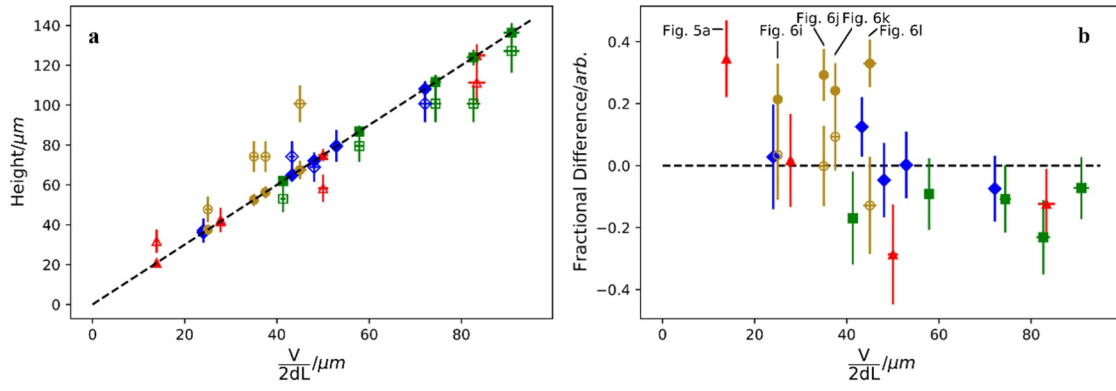
Figure 7. (Colour online) Comparison of measured and predicted maximum heights for four different confinement dimensions: 6 × 6 mm (red triangles), 11 × 11 mm (green squares), 16 × 13 mm (blue diamonds), 20 × 10 mm (gold circles). (a) Maximum height predicted from the models (closed data points) plotted with respect to the height measured using the number of birefringent fringes (open data points). A black line of the expected $y = \frac{3}{2}x$ (Equation (1)) is added to further validate the models. (b) Fractional difference between the measured and predicted maximum heights assuming no deviation from the expected d and L values (closed data points). For a selection of samples with less good agreement between the measured and predicted heights, heights are calculated using the same models, but with a measured d and L to reflect the true NLC area (open data points). The corresponding polarised light images where this comparison is completed are marked on the figure. $\frac{V}{2dL}$ is calculated using the known d and L, allowing for a clear comparison. A dashed line is added at y = 0 for ease of analysis.

L values moves the points for these four samples closer to the fractional difference = 0 dashed line.

A second possible reason for the discrepancies in the measured and predicted heights is that the assumption that the semi-droplet cross-sectional area is a minor segment of a circle is incorrect. Figure 8 directly compares the measured and predicted heights across the semi-droplets for three relatively small heights (measured heights between 32 and 130 µm) for each of the four confinement dimensions. Equations (1) and (2) are fitted to the measured heights, where the cross-sectional area and interface angle, respectively, are allowed to vary. It can be seen that the models are indistinguishable for this parameter space and that there is an excellent fit for the semi-droplets with the smallest heights, but that the actual shapes of the semi-droplets deviate from the model as the height increases. In particular, for the semi-droplet profiles with greater heights, the centres are flatter and there is more curvature at the edges. We suggest that this distortion can be attributed to the effect of gravity as neither model includes gravitational terms, and the height is much smaller than the width in all cases, so it is to be expected that the middle region will be relatively flattened.

Ensuring that the geometry is smaller than the capillary length allows us to make the assumption that gravitational effects can be neglected; for E7, $L_C \sim 1.57$ mm. In this work $d > L_C$, i.e for the 6 mm square confinements, $\frac{d}{L_c} \sim 1.91$; for the 20 × 10 mm rectangles, $\frac{d}{L_c} \sim 3.18$; for the 11 mm squares, $\frac{d}{L_c} \sim 3.5$, and for the 16 × 13 mm rectangles, $\frac{d}{L_c} \sim 4.14$, i.e. we have relaxed

this important constraint in the expectation that the semi-droplets will be more readily visible without the need for a microscope. We find qualitatively that for heights ≲ 50 µm, the fits of the models to the data in Figure 8 are in good agreement, regardless of the ratio of the semi-droplet half-width to the capillary length.

Figure 9, like Figure 8, compares the measured and predicted heights of the semi-droplets, however along their lengths (y-axis). A common feature in the measured heights for Figures 8 and 9 is their asymmetry, as shown relative to the dashed line at x = 0. As no special effort was made to ensure the stage of the imaging system was perfectly flat, there was probably a tilt of a few degrees in the x- and y-axes, which would explain this asymmetry due to gravity, but does not have a significant or adverse effect on the semi-droplets. When the semi-droplets are imaged, they are in a steady state. The asymmetry is most clearly seen both along the width and length for a measured height = 101 µm for the 20 × 10 mm samples (Figures 8 and 9 (d)), with the polarised light image in Figure 6(l). Along the length for the rectangles, there is a clear increase of asymmetry for the rectangles as compared to the squares, with the 6 mm square , generally, the most symmetric. It is to be expected that a more asymmetric shape of the NLC is possible in the lower aspect ratio rectangles; the squares have an aspect ratio of 1, whereas the rectangles have aspect ratios of approximately 0.8 for the 16 × 13 mm and 0.5 for the 20 × 10 mm rectangles. It is also to be expected that the shape is less symmetric along the length of the rectangular samples,
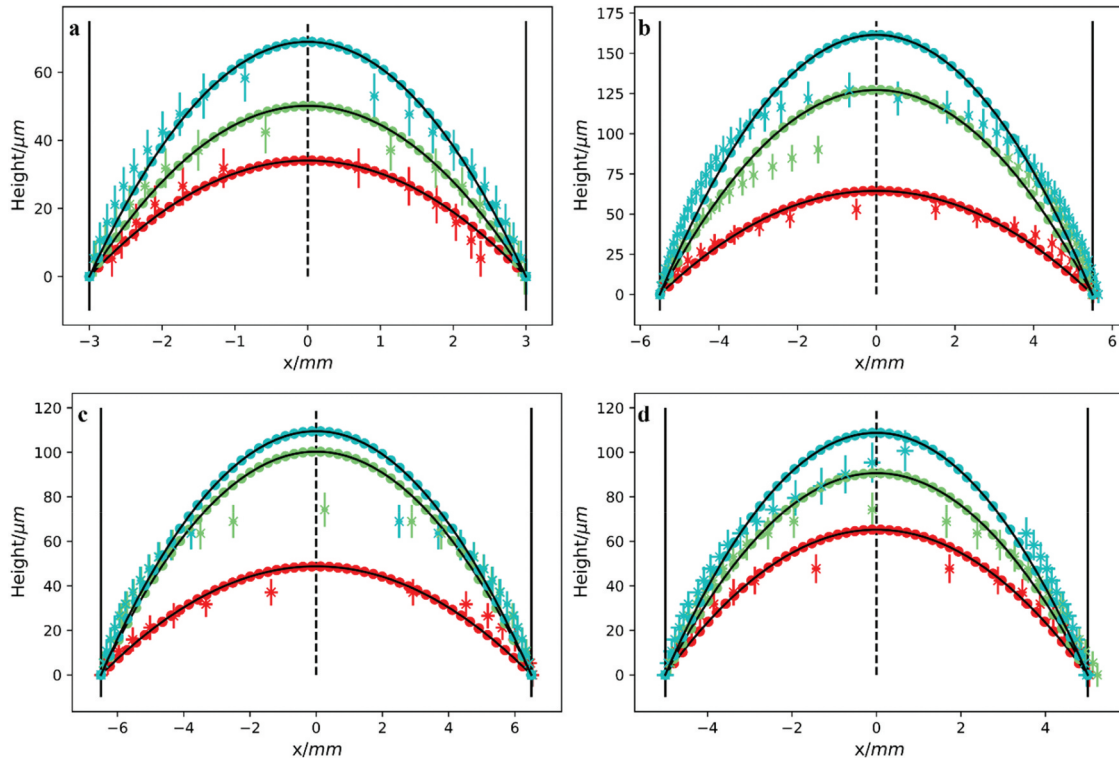
Figure 8. (Colour online) Height variation using the centre-to-centre distances of pink birefringent fringes across NLC semi-droplet widths for three NLC dispense volumes, V, and four confinement sizes: (a) 6 × 6 mm with V = 0.5 μL (red), 1 μL (green), 1.8 μL (blue). (b) 11 × 11 mm with V = 5 μL (red), 10 μL (green), 11 μL (blue). (c) 16 × 13 mm with V = 5 μL (red), 9 μL (green), 10 μL (blue). (d) 20 × 10 mm with V = 5 μL (red), 7 μL (green), 9 μL (blue). The data is fitted to both Equation (2) (black line), and Equation (1) (circles). A dashed line is included at x = 0, as well as solid lines at the expected edges of the confinement shapes.
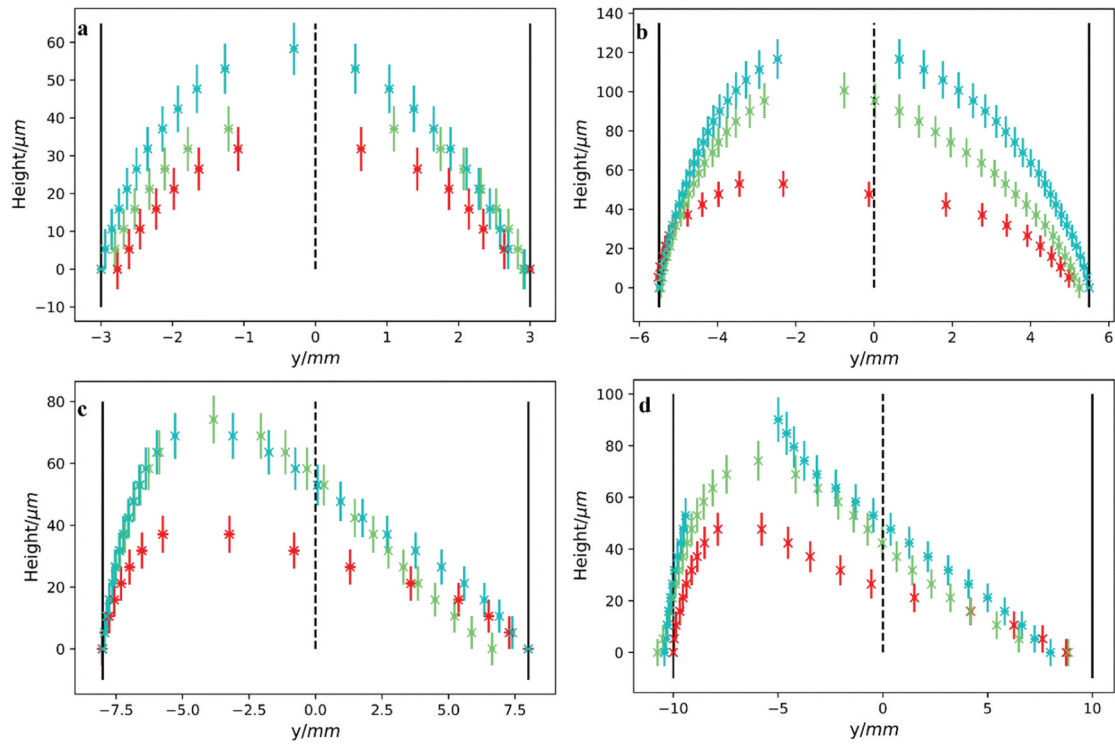

Figure 9. (Colour online) Height variation using the centre-to-centre distances of the pink birefringent fringes across NLC semi-droplet lengths for three NLC dispense volumes, V, and four confinement sizes: a) 6 × 6 mm with V = 0.5 μL (red), 1 μL (green), 1.8 μL (blue). (b) 11 × 11 mm with V = 5 μL (red), 10 μL (green), 11 μL (blue). (c) 16 × 13 mm with V = 5 μL (red), 9 μL (green), 10 μL (blue). (d) 20 × 10 mm with V = 5 μL (red), 7 μL (green), 9 μL (blue).

especially in the longest samples (20 × 10 mm), as the increased length will allow for gravity to have a larger effect on the symmetry of the semi-droplet.

The solid black lines at the edge of the plots indicate the expected values for x = ± d (Figure 8) or y = ± $\frac{L}{2}$ (Figure 9) and allow us to consider the quality of filling of the semi-droplet within the confinements. All the samples presented in Figure 8 demonstrate a good agreement with these lines, except for those with measured heights = 130 μm for the 11 mm square confinement, and measured height = 74 μm for the 16 × 13 mm rectangle confinement (Figure 8(b,d), with the polarised light images in Figure 6(c,j), respectively). In the x-axis, they are overfilled by 0.15 ± 0.08 mm and 0.2 ± 0.1 mm, respectively; hence, there are only slight differences with the measured and expected sample edges, indicating that there is overall good filling along the width of the confinement. For Figure 9, the 20 × 10 mm size confinements (Figure 9(d)) are the only examples given with significant under- or overfilling. For Figure 6(i) (measured height = 48 μm) this corresponds to an underfill at the top of the confinement (positive x-axis in Figure 9) of 1.2 ± 0.1 mm; for Figure 6(j) (measured height = 74 μm), there is an overfill at the bottom of the confinement (negative x-axis in Figure 9) of 0.8 ± 0.1 mm, and an underfill at the top of 1.1 ± 0.1 mm, and for Figure 6(l) (measured height = 101 μm) the overfill at the bottom is 0.4 ± 0.2 mm and the underfill at the top is 2.0 ± 0.2 mm. Therefore, this size can be ruled out as a choice for useful sensing devices in the future. In general, for the other confinement sizes (Figure 9(a-c)) there is good filling along the length.

Defect formation in NLC semi-droplets

A key consideration of use of this system as a sensor is how clear and reproducible the director fields are before the addition of the analyte. A common feature of NLC confined on a stripe surface seen in the literature is a central disclination line. For example, in Bao *et al.* [38], a central disclination is described by an 'escaped radial' director field, characterised by alternating defects of strength of ±1. Cousins *et al.* [39] describe the central disclination line observed in their work in terms of a discontinuous angle of the NLC director. A similar feature is seen in each of the polarised light images in Figures 5, 6 and S3, i.e. a disclination line, or line of defects that runs approximately perpendicular to the rubbing direction. This is most consistent in the 6 mm square

and is the straightest in the V = 7 μL (predicted height = 290 μm, Figure 5(f)) sample, although samples such as V = 5 μL in a 6 mm square (predicted height = 208 μm, Figure 5(e)) have a similar level of quality.

As already discussed, the square confinement shapes (Figure 9(a,b)) have a generally more symmetric filling than the rectangles (Figure 9(c,d)). Examples from Figures 5, 6 and S3 demonstrate, however, that there is a balance to be found for the NLC dispense volume so as not to overfill (e.g. Figure 5(h)) or underfill (e.g. Figure 5(a)) the samples. Significant overfilling could impact the quality of the director field significantly for example, in Figure 6(d) (with a predicted height = 370 μm) has extra domains other than the central disclination line. As the 6 mm square confinement was identified as having the straightest central disclination line in general, it should be the focus for identifying the correct volume of the semi-droplet. i.e. qualitatively between V = 3–5 μL corresponding to predicted heights = 125–208 μm (Figure 5(d,e)) offer a uniform filling, including to the corners of the confinement, but without overfilling it, suggesting a good choice of parameter space to continue development for sensors.

These key points, i.e. how straight the central defect line is, as well as the quality and symmetry of the filling imply that the 6 mm square with V ∼ 3–7 μL is the most suitable for future sensor development. There are clear benefits to this finding, in that less liquid crystal will need to be used to fill the sample than would be needed in a larger confinement size or a higher dispense volume, however a balance must be found between usage of material and sensitivity of the sample. For example, whilst Bao *et al.* [38] present a sample with a straighter central disclination line, the width of their stripes was of the order of μm instead of mm as in this work, hence may well be less sensitive to gaseous stimuli and would have to be viewed using a microscope.

The polarised light images in Figures 5, 6 and S3 suggest that the chemically patterned surfaces used are reusable and reproducible, as a maximum of two different surfaces for each confinement size were used to collect the data and were washed off with IPA in-between refilling with NLC to form the semi-droplets and imaging. There is no significant variation in the director field or quality seen in the polarised light images other than those discussed in relation to the volume dispensed and confinement dimensions, therefore this system could lead to more sustainable future sensing methods, as well as make for safer usage due to IPA being a relatively safe and cheap solvent.

Interface angle

As was mentioned earlier, the interface angle is a powerful parameter as it can allow many other semi-droplet parameters to be predicted including maximum height and height variation along the semi-droplet width (Equation (2)) as well as the radius of the circle on which the semi-droplets are modelled (Figure 2, Equation (4)). In the results and discussion sections, it was determined that the 6 mm squares have the best potential for future work on sensing devices. Therefore, the 6 × 6 mm square confinements for V = 0.5–1.8 μL (Figure 5(a–c)) are used to investigate the validity of the interface angles predicted from the models, as given in Table 1(b) (i.e. using V = AL to deduce the cross-sectional area, followed by Equation (1) to predict ε, and Equation (3) to predict θ_I). Measurements of the interface angle, Table 1(c), were made by applying a linear fit to the first few data points on the left of Figure 8(a). All the interface angles presented in Table 1(b,c) are < 4° which highlights one aspect of why the models presented simplify the prediction of the interface angle and hence the prediction of the height variation across the semi-droplet. i.e. this angle would be difficult to measure directly and accurately using contact angle apparatus.

The measured interface angle (Table 1(d)) is always greater than the predicted interface angle (Table 1(c)), as would be expected from examination of the experimental data and models in Figure 8(a). There are two contributions to this observation. Firstly, the predicted value of θ_I, having only the uncertainties in V, d and L which are small, is likely to be quite accurate, whereas the measurement relies only on a few data points, and the linear fit is only an approximation of the shape. To determine whether the interface angle deduced from measurements or the model is better at predicting the semi-droplet height, Table 1 also compares calculations (d and e, respectively) with measurements (f). For the V = 0.5 μL sample, the predicted height from the measured interface angle is significantly closer to the measured

height than the predicted height from the predicted interface angle. However, the inverse is seen for the V = 1 μL and 1.8 μL samples, though neither agrees particularly well in the case of a larger volume.

The radius of the circle used to model the semi-droplets (Figure 2) can be calculated using the predicted interface angle with Equation (4) and is shown in Table 1(g). The fact that the radius is approximately three orders of magnitude larger than the heights further validates the use of the HAN director field (Figure 4(c)) that was assumed in this work to describe the director along the NLC semi-droplet height.

Conclusions

NLC-based chemical sensing is a growing research area. Here, a novel chemical patterning method has been used to create rectangles with accurately known dimensions on a surface to confine NLC, forming relatively large NLC semi-droplets. These all have a well-defined hybrid alignment due to one rubbed planar surface (solid substrate) and one homeotropic surface (NLC/air). The fabricated rectangles cover a wide dimensional range with widths between 6 and 13 mm, lengths between 6 and 20 mm, and aspect ratios between 0.5 and 1. The confined NLC semi-droplets had a range of heights between ~20 and 420 μm. This work has therefore investigated a significant range of variables, allowing a better understanding of the limiting factors in the parameter spaces in context of a future sensing device. The lack of a significant change in quality in the polarised light images noted when reusing the confinement surfaces *via* washing with IPA in-between imaging and refilling with NLC suggests that the surfaces are reusable, which is beneficial for a potentially rapid, multi-use sensor system.

A simple model to describe the height of the NLC across the stripe was derived and compared to an existing, more detailed model. The two models had a similar experimental and theoretical geometry, however the

Table 1. Parameters determined from measurements or predictions for (a) three NLC volumes of 6 x 6 mm squares. (b) The predicted interface angle from calculating V = AL, estimating ε (Equation (1)), and finally Equation (3). (c) The interface angle measured from linear fits of the first few data points on the left-hand side of the height variation plots in Figure 8(a). (d) The measured heights in the polarised light images (Figures 5(a-c)). (e) The heights predicted using Equation (2) from the θ in (b). The heights predicted using Equation (2) from the θ in (c). (g) The radius of the circle on which the simple geometric model is based (Figure 2).

(a)	(b)	(c)	(d)	(e)	(f)	(g)
NLC Volume, V/μL	Predicted (Model) θ_I/°	Measured (Linear fit) θ_I/°	Height from predicted θ_I (b)/μm	Height from measured θ_I (c)/μm	Measured height, h/μm	Predicted radius, r, from θ_I (b)/mm
0.5 ± 0.01	0.80 ± 0.03	1.32 ± 0.06	21 ± 1	35 ± 2	32 ± 6	220 ± 10
1 ± 0.01	1.59 ± 0.07	2.3 ± 0.1	42 ± 2	60 ± 3	42 ± 6	108 ± 5
1.8 ± 0.01	2.9 ± 0.1	3.7 ± 0.2	75 ± 3	98 ± 5	58 ± 7	60 ± 3

model in this work is calculated using the interface angle, while the existing model utilises the cross-sectional area. Therefore, a combination of the two models allows for the cross-sectional area (estimated using the volume of the semi-droplet and assuming that the cross-sectional area is constant along its length) to give a prediction of the interface angle. This in turn can be used to predict the height variation across the semi-droplet, as well as the maximum height. These predictions were found to be in excellent agreement with experimentally measured semi-droplet heights, found from the birefringent fringes of the NLC polarised light images, lending validation to the model. The height variation was deduced across the whole semi-droplet width, whereas Cousins et al. [39] evaluated this at the semi-droplet edge. Systematic differences such as the effect of under- or over-filling the confinements and the potential effect of gravity were discussed. It was shown that the height of the NLC in semi-droplets is both more symmetric in the width – rather than length – direction, and that the squares, particularly the 6 mm square, were most symmetric. The model was found to agree well with measurements for heights $\lesssim$ 50 μm, even though the dimensions exceeded the capillary length of the NLC, $\frac{d}{L_c} > 1$, irrespective of the value of the ratio $\frac{d}{L_c} \sim 1.91–4.14$.

The 6 mm square was seen to exhibit a more well-defined, straight, and central defect line (a feature commonly seen in NLC semi-droplets) than the 11 mm square or rectangular confinements. The study has also shown that there must be enough NLC to fill the sample but not so much to overfill it or to cause a decrease in the quality of the director field by causing extra domains to form in the semi-droplet. Of the samples investigated, the V ~ 2–7 μL-filled 6 mm squares, with predicted heights between ~125 and 290 μm demonstrated the best director field of those presented for simplicity and reproducibility as a sensor. Combined with the good symmetry as previously discussed, the 6 mm square is suggested to be a good parameter space for future sensing work.

Notes

1. Nissan Chemical Industries Ltd. Data sheet for 'Alignment Coatings for LCDs-SUNEVER Series' −1/2
2. See Synthon Chemicals Safety Data Sheet for 'Liquid crystal Mixture E7'.

Acknowledgments

Disclosure statement

Funding

ORCID

Abigail Bond http://orcid.org/0009-0005-4998-1211
Thomas Moorhouse http://orcid.org/0000-0001-7319-9549
Sally A. Peyman http://orcid.org/0000-0002-1600-5100
Helen F. Gleeson http://orcid.org/0000-0002-7494-2100

Data

The data associated with this paper can be found at DOI: https://doi.org/10.5518/1606

References

[1] Goodby JW, Collings PJ, Kato T, et al., editors. Handbook of liquid crystals. Second. Boschstr. completely revised and greatly enlarged. Vol. 12, Weinheim, Germany: Wiley-VCH. Verlag GmbH & Co. KGaA; 2014. p. 69469.

[2] Gupta VK, Skaife JJ, Dubrovsky TB, et al. Optical amplification of ligand-receptor binding using liquid crystals. Science. 1998;279(5359):2077–2080. doi: 10.1126/science.279.5359.2077

[3] Zhan X, Liu Y, Yang KL, et al. State-of-the-art development in liquid crystal biochemical sensors. Biosensors (Basel). 2022;12(8):12. doi: 10.3390/bios12080577

[4] Wang H, Xu T, Fu Y, et al. Liquid crystal biosensors: principles, structure and applications. Biosensors (Basel). 2022;12(8):639. doi: 10.3390/bios12080639

[5] Schenning APHJ, Crawford GP, Broer DJ, editors. Liquid crystals sensors. Boca Raton, London and New York.: CRC Press. Taylor & Francis Group; 2017.

[6] Bao P, Paterson DA, Harrison PL, et al. Lipid coated liquid crystal droplets for the on-chip detection of antimicrobial peptides. Lab Chip. 2019;19(6):1082–1089. doi: 10.1039/C8LC01291A

[7] Deng J, Liang W, Rhodes S, et al. Influence of polymer networks on the sensor properties of hydrogel dispersed liquid crystal droplets. Colloids Surf A. 2019;570:438–443. doi: 10.1016/j.colsurfa.2019.03.066

[8] Paterson DA, Bao P, Abou-Saleh RH, et al. Control of director fields in phospholipid-coated liquid crystal

droplets. Langmuir. 2020;36(23):6436–6446. doi: 10. 1021/acs.langmuir.0c00651

[9] Jiang S, Noh J, Park C, et al. Using machine learning and liquid crystal droplets to identify and quantify endotoxins from different bacterial species. Analyst. 2021;146:1224–1233.

[10] Paterson DA, Du X, Bao P, et al. Chiral nematic liquid crystal droplets as a basis for sensor systems. Mol Syst Des Eng. 2022;7(6):607–621. doi: 10.1039/D1ME00189B

[11] Piñeres-Quiñones OH, Lynn DM, Acevedo-Vélez C. Environmentally responsive emulsions of thermotropic liquid crystals with exceptional long-term stability and enhanced sensitivity to aqueous Amphiphiles. Langmuir. 2022;38(3):957–967. doi: 10.1021/acs.langmuir.1c02278

[12] Xie S, He R, Zhu Q, et al. Label-free optical sensor based on liquid crystal sessile droplet array for penicillin G determination. Colloids urf A. 2022;644:128728.

[13] Zhang G, Zhu A, Wang S, et al. Stabilizing liquid crystal droplets with hydrogel films and its application in monitoring adenosine triphosphate. Colloids Surf A. 2022;654:130122. doi: 10.1016/j.colsurfa.2022.130122

[14] Aery S, Parry A, Araiza-Calahorra A, et al. Ultra-stable liquid crystal droplets coated by sustainable plant-based materials for optical sensing of chemical and biological analytes. J Mater Chem C. 2023;11(17):5831–5845. doi: 10.1039/D3TC00598D

[15] Zhang G, Zhao W, Liu W, et al. A cytidine-modified surfactant anchored liquid crystal droplet-based sensor for rapid and accurate detection of silver ions. J Colloid Interface Sci. 2023;650:58–66. doi: 10.1016/j.jcis.2023.06.111

[16] Honaker LW, Eijffius A, Plankensteiner L, et al. Biosensing with oleosin-stabilized liquid crystal droplets. Small. 2024;20(31):2309053. doi: 10.1002/smll.202309053

[17] Ren H, An Z, Jang C-H. Liquid crystal-based aptamer sensor for sensitive detection of bisphenol a. Microchem J. 2019;146:1064–1071. doi: 10.1016/j.microc.2019.02.019

[18] Yang X, Li H, Zhao X, et al. A novel, label-free liquid crystal biosensor for Parkinson's disease related alpha-synuclein. Chem Commun. 2020;56(40):5441–5444. doi: 10.1039/D0CC01025A

[19] Nguyen DK, Jang C-H. A label-free liquid crystal bio-sensor based on specific DNA aptamer probes for sensitive detection of amoxicillin antibiotic. Micromachines. 2021;12(4):370. doi: 10.3390/mi12040370

[20] Chang T-K, Lee M-J, Lee W. Quantitative biosensing based on a liquid crystal marginally aligned by the PVA/DMOAP composite for optical signal amplification. Biosensors (Basel). 2022;12(4):218. doi: 10.3390/bios12040218

[21] Pourasl MH, Vahedi A, Tajalli H, et al. Liquid crystal-assisted optical biosensor for early-stage diagnosis of mammary glands using HER-2. Sci Rep. 2023;13(1):6847. doi: 10.1038/s41598-023-31668-8

[22] Soares MS, Sobral RG, Santos N, et al. Liquid crystal-based immunosensor for the optical detection of Escherichia Coli at low concentration levels. IEEE Sens J. 2024;24:8848–8856.

[23] Wang S, Zhang G, Chen Q, et al. Sensing of cocaine using polarized optical microscopy by exploiting the conformational changes of an aptamer at the water/liquid crystal interface. Microchim Acta. 2019;186 (11):724. doi: 10.1007/s00604-019-3855-1

[24] Ho TY, Huang J-W, Peng B-C, et al. Liquid crystal-based sensor system for detecting formaldehyde in aqueous solutions. Microchem J. 2020;158:105235. doi: 10.1016/j.microc.2020.105235

[25] Sun H, Yin F, Liu X, et al. Development of a liquid crystal-based α-glucosidase assay to detect anti-diabetic drugs. Microchem J. 2021;167:106323.

[26] Cheng S, Khan M, Yin F, et al. Liquid crystal-based sensitive and selective detection of uric acid and uricase in body fluids. Talanta. 2022;244:123455. doi: 10.1016/j.talanta.2022.123455

[27] Song H, Khan M, Yu L, et al. Construction of liquid crystal-based sensors using enzyme-linked dual-functional nucleic acid on magnetic beads. Anal Chem. 2023;95(35):13385–13390. doi: 10.1021/acs.analchem.3c03163

[28] Lalitha R, Mondal S. Liquid crystal-based label-free low-cost sensing platform: engineering design based on interfacial interaction and transport phenomena. Colloids Surf A. 2024;682:132986. doi: 10.1016/j.colsurfa.2023.132986

[29] Yu H, Liu X, Sun W, et al. A brief review of whispering gallery mode in sensing. Opt Laser Technol. 2024;177:111099. doi: 10.1016/j.optlastec.2024.111099

[30] Liu Z, Luo D, Yang K-L. Monitoring the two-dimensional concentration profile of toluene vapors by using polymer-stabilized nematic liquid crystals in microchannels. Lab Chip. 2020;20(9):1687–1693. doi: 10.1039/C9LC01021A

[31] Shin MJ, Yoon DK. Role of stimuli on liquid crystalline defects: from defect engineering to switchable functional materials. Materials. 2020;13(23):13. doi: 10.3390/ma13235466

[32] Bramble JP, Evans SD, Henderson JR, et al. Nematic liquid crystal alignment on chemical patterns. Liq Cryst. 2007;34(9):1059–1069. doi: 10.1080/02678290701614665

[33] Ohzono T, Monobe H, Shiokawa K, et al. Shaping liquid on a micrometre scale using microwrinkles as deformable open channel capillaries. Soft Matter. 2009;5:4658–4664.

[34] Anquetil-Deck C, Cleaver DJ. Nematic liquid-crystal alignment on stripe-patterned substrates. Phys Rev E. 2010;82(3):031709. doi: 10.1103/PhysRevE.82.031709

[35] Ohzono T, Fukuda J-i. Transition of frustrated nematic order and fluctuation of topological defects in micro-wrinkle grooves. Soft Matter. 2012;8(45):11552–11556. doi: 10.1039/c2sm26701b

[36] Ohzono T, Fukuda J-i. Zigzag line defects and manipulation of colloids in a nematic liquid crystal in microwrinkle grooves. Nat Commun. 2012;3(1):701. doi: 10.1038/ncomms1709

[37] Choi Y, Yokoyama H, Gwag JS. Determination of surface nematic liquid crystal anchoring strength using nano-scale surface grooves. Opt Express. 2013;21 (10):12135–12144. doi: 10.1364/OE.21.012135

[38] Bao P, Paterson DA, Peyman SA, et al. Textures of nematic liquid crystal cylindric-section droplets confined by chemically patterned surfaces. Crystals. 2021;11(1):65. doi: 10.3390/cryst11010065

[39] Cousins JRL, Bhadwal AS, Corson LT, et al. Weak-anchoring effects in a thin pinned ridge of nematic liquid crystal. Phys Rev E. 2023;107(3):034702. doi: 10.1103/PhysRevE.107.034702

[40] Pawale T, Swain J, Hashemi MR, et al. Dynamic motions of topological defects in nematic liquid crystals under spatial confinement. Adv Mater Interface. 2023;10:2300136.

[41] Cousins JRL, Duffy BR, Wilson SK, et al. Young and Young–Laplace equations for a static ridge of nematic liquid crystal, and transitions between equilibrium states. Proc R Soc A. 2022;478 (2259):20210849. doi: 10.1098/rspa.2021.0849

[42] de Gennes PG. Wetting: statics and dynamics. Rev Mod Phys. 1985;57(3):827–863. doi: 10.1103/RevModPhys.57.827

[43] Amalathas AP, Alkaisi MM. Fabrication and replication of periodic nanopyramid structures by laser interference lithography and UV nanoimprint lithography for solar cells applications. In: Jagannathan T, editor. Micro/Nanolithography - A heuristic aspect on the enduring technology. London, UK: IntechOpen; 2018. p. 30–32. Ch. 2.

[44] Munief W-M, Heib F, Hempel F, et al. Silane deposition via gas-phase evaporation and high-resolution surface characterization of the ultrathin siloxane coatings. Langmuir. 2018;34:10217–10229.

[45] Allinson H, Gleeson HF. Physical properties of mixtures of low molar mass nematic liquid crystals with photochromic fulgide guest dyes. Liq Cryst. 1993;14:1469–1478.